

# Lawrence Berkeley National Laboratory

## LBL Publications

### Title

Equally high efficiencies of organic solar cells processed from different solvents reveal key factors for morphology control

### Permalink

<https://escholarship.org/uc/item/52q8x8ts>

### Authors

Zhang, Rui

Chen, Haiyang

Wang, Tonghui

et al.

### Publication Date

2024-12-04

### DOI

10.1038/s41560-024-01678-5

### Copyright Information

This work is made available under the terms of a Creative Commons Attribution License, available at <https://creativecommons.org/licenses/by/4.0/>

Peer reviewed

# Equally high efficiencies of organic solar cells processed from different solvents reveal key factors for morphology control

Received: 20 February 2024

Accepted: 28 October 2024

Published online: 04 December 2024

Check for updates

Rui Zhang<sup>1</sup>, Haiyang Chen<sup>2</sup>, Tonghui Wang<sup>3</sup>✉, Libor Kobera<sup>4</sup>, Lilin He<sup>5</sup>, Yuting Huang<sup>2</sup>, Junyuan Ding<sup>2</sup>, Ben Zhang<sup>2</sup>, Azzaya Khasbaatar<sup>6</sup>, Sadisha Nanayakkara<sup>7</sup>, Jialei Zheng<sup>2</sup>, Weijie Chen<sup>2</sup>, Ying Diao<sup>6,8</sup>, Sabina Abbrent<sup>4</sup>, Jiri Brus<sup>4</sup>, Aidan H. Coffey<sup>9</sup>, Chenhui Zhu<sup>9</sup>, Heng Liu<sup>10</sup>, Xinhui Lu<sup>10</sup>, Qing Jiang<sup>3</sup>, Veaceslav Coropceanu<sup>7</sup>, Jean-Luc Brédas<sup>7</sup>, Yongfang Li<sup>2,11</sup>, Yaowen Li<sup>2</sup>✉ & Feng Gao<sup>1,12</sup>✉

The power conversion efficiency of organic solar cells (OSCs) is exceeding 20%, an advance in which morphology optimization has played a significant role. It is generally accepted that the processing solvent (or solvent mixture) can help optimize morphology, impacting the OSC efficiency. Here we develop OSCs that show strong tolerance to a range of processing solvents, with all devices delivering high power conversion efficiencies around 19%. By investigating the solution states, the film formation dynamics and the characteristics of the processed films both experimentally and computationally, we identify the key factors that control morphology, that is, the interactions between the side chains of the acceptor materials and the solvent as well as the interactions between the donor and acceptor materials. Our work provides new understanding on the long-standing question of morphology control and effective guides to design OSC materials towards practical applications, where green solvents are required for large-scale processing.

The history of organic solar cells (OSCs) has been dominated by the development of donor and acceptor materials and by the optimization of the morphology of the donor/acceptor active layers (bulk heterojunctions), which has led to high power conversion efficiencies (PCEs) exceeding 20% (certified for 19.2% from National Renewable Energy Laboratory (NREL))<sup>1–3</sup>. These high efficiencies, combined with their specific features (for example, lightweight, easy fabrication, facile colour tunability)<sup>4–6</sup>, make OSCs promising candidates for next-generation photovoltaic technologies<sup>7–9</sup>.

Along with the efficiency breakthrough, there have also been extensive investigations aiming to provide design rules for materials and morphology development. The connection between materials characteristics and device performance has become much better

understood as a result of effective strategies to broaden the absorption spectra, tune the energies of the relevant electronic states and optimize charge transport<sup>10–12</sup>. Understanding the link between bulk heterojunction morphology and device performance is challenging as it involves the connection with the ultrafast charge-transfer and charge-recombination processes taking place between the electron-donating (donor) and electron-accepting (acceptor) systems<sup>13–16</sup>. A set of morphological manipulation strategies and techniques has been developed to improve the efficiency of physical processes such as exciton diffusion, charge dissociation, charge recombination, charge transport and charge extraction<sup>17–20</sup>. In solution-processed blends, optimization in the choice of solvents and additives has played a key role in improving OSC efficiencies as it

A full list of affiliations appears at the end of the paper. ✉ e-mail: [twang@jlu.edu.cn](mailto:twang@jlu.edu.cn); [ywli@suda.edu.cn](mailto:ywli@suda.edu.cn); [feng.gao@liu.se](mailto:feng.gao@liu.se)

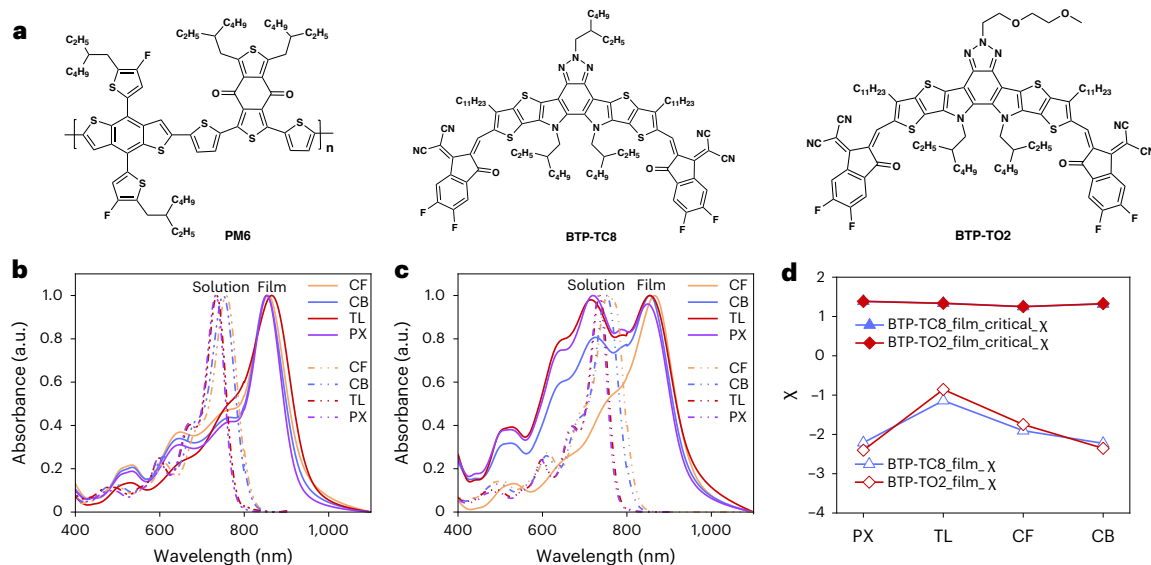


**Fig. 1 | Chemical structures, absorption spectra in various solvents and molecular dynamics calculations of Flory–Huggins interaction parameters.**

**a.** Chemical structures of PM6, BTP-TC8 and BTP-TO2. **b.** Solution (concentration of 20 mg ml<sup>-1</sup>) and film absorption spectra for BTP-TO2 considering various solvents: chloroform (CF), chlorobenzene (CB), toluene (TL), p-xylene (PX).

**c.** Solution (concentration of 20 mg ml<sup>-1</sup>) and film absorption spectra for BTP-TC8 considering the same solvents. **d.** AA-MD simulated Flory–Huggins interaction parameters,  $\chi$ , of BTP-TC8 and BTP-TO2 in CF, CB, TL and PX solutions at concentrations of 20 mg ml<sup>-1</sup>.

allowed fine tuning of the donor and acceptor domain sizes and control of the crystalline kinetic processes of the components<sup>21–23</sup>. Post thermal/solvent annealing processes provide additional driving forces for manipulating the molecular self-assembly,  $\pi$ – $\pi$  packing behaviours and relative molecular orientations<sup>24,25</sup>. The influence of component sequential deposition<sup>26,27</sup>, pseudo-bilayer architecture<sup>28</sup> and ternary strategies<sup>29,30</sup> in controlling domain purity, component interfaces and intermolecular interactions<sup>31</sup> has also been documented.

Despite these advances, an understanding of the morphological features and their manipulation strategies has often been restricted to specific systems, a limitation that persists even for derivatives of similar materials with minimal modifications<sup>32,33</sup>. There have been efforts moving one step further, aiming to rationalize how the film morphology is impacted by the aggregation behaviour of the components in solution<sup>34–36</sup>. However, these investigations on solution aggregation have primarily focused on micro-scale aspects, whereas the relevant photophysical processes determining charge separation and recombination happen at the nano-scale and molecular levels. Consequently, it remains challenging to develop a description of effective principles to control morphology in different OSC blends (for example, PM6:Y6 devices display 12.15% PCE when chlorobenzene processed but 16.88% PCE when chloroform processed<sup>37</sup>), impeding the commercial scalability (and hence industrial applications) of OSCs.

In this work, we provide a comprehensive picture of the fundamental factors that determine the OSC morphology. We develop a novel acceptor material BTP-TO2 incorporating an oligo (ethylene glycol) (OEG) side chain attached to the central nitrogen atom of its benzotriazole unit (Fig. 1a). We demonstrate that BTP-TO2 leads to similar active layer morphology when processed from a wide range of (halogenated and non-halogenated) solvents and consistently contributes to high PCEs around 19%. By examining both the intrinsic molecular conformations and the interactions in solution and film states at the nano-scale level, we can propose general morphological design rules for non-fullerene-based OSC blends: to enhance the interaction between the side chain of the non-fullerene acceptors (NFAs) and the solvent to ensure that acceptors maintain a stable and persistent molecular conformation in various solutions; to weaken the intermolecular interactions between the polymer donor and the NFA in

solution, to promote the rod-like conformation of the polymer donor and its preferential precipitation, ensuring that the film formation dynamics have little impact on the blend film morphology. Building upon the foundational knowledge derived from our successful case study, we further generalize our morphological design rules by developing an additional non-fullerene acceptor, which also demonstrates solvent-independent morphology and device performance.

## Molecular aggregation and conformation in solution

OEG side chains, with their hydrophilicity, polarity and flexibility properties, are instrumental in defining the molecular conformation, solubility and self-assembly characteristics of conjugated polymers and small-molecule semiconductors that carry them<sup>38,39</sup>. In this context, as the primary subject of our discussion, we developed a novel NFA BTP-TO2 (Fig. 1a), 2,2'-(2Z,2'Z)-((12,13-bis(2-ethylhexyl)-6-(2-(2-methoxyethoxy)ethyl)-3,9-diundecyl-12,13-dihydro-6H-thieno[2',3':4',5']thieno[2',3':4',5]pyrrolo[3,2-g]thieno[2',3':4',5]thieno[3,2-b][1,2,3]triazolo[4,5-e]indole-2,10-diyl)bis(methanylylidene))bis(5,6-difluoro-3-oxo-2,3-dihydro-1H-indene-2,1-diylidene))dimalononitrile. This strategic modification is designed to expand the scope of interactions between the small-molecule acceptors and organic solvents, a point that will be discussed in detail below. In-depth descriptions of synthesis processes, molecular structure, molecular weight characterizations (including nuclear magnetic resonance (NMR) spectra and matrix-assisted laser desorption/ionization time-of-flight (MALDI-TOF) spectroscopy) and thermal gravimetric analysis thermograms can be found in Supplementary Figs. 1–5. BTP-TO2 exhibits exceptional stability, as evidenced by its decomposition temperature that surpasses 340 °C. Electrochemical cyclic voltammetry (CV) measurements demonstrate that the ionization energy (that is, roughly speaking, the highest occupied molecular orbital energy) and electron affinity (lowest unoccupied molecular orbital energy) of BTP-TO2 match closely those of 2,2'-(2Z,2'Z)-((6,12,13-tris(2-ethylhexyl)-3,9-diundecyl-12,13-dihydro-6H-thieno[2',3':4',5']thieno[2',3':4',5]pyrrolo[3,2-g]thieno[2',3':4',5]thieno[3,2-b][1,2,3]triazolo[4,5-e]indole-2,10-diyl)bis(methanylylidene))bis(5,6-difluoro-3-oxo-2,3-dihydro-1H-indene-2,1-diylidene))dimalononitrile (BTP-TC8) (Supplementary Fig. 6 and

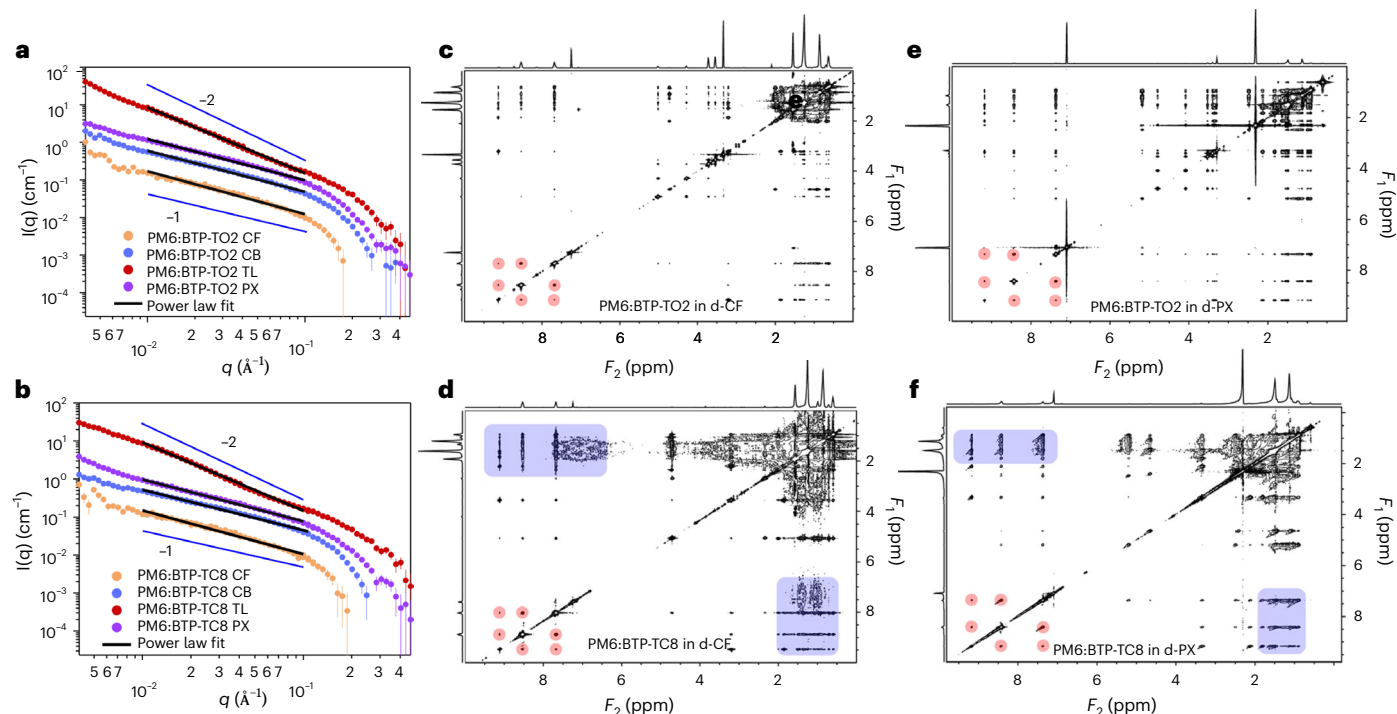


**Fig. 2 | Solution states and intermolecular interactions between components in PM6:BTP-TC8 and PM6:BTP-TO2 mixtures.** **a, b**, SANS spectra with fractal dimension analysis for PM6:BTP-TC8 and PM6:BTP-TO2 in deuterated solutions, where the donor:acceptor ratio is 1:1.2 (w/w, 11.5 mg ml<sup>-1</sup> of donor). The flexible cylinder model is used to fit the curves: In the intermediate  $q$  region (0.005 to 0.1 Å<sup>-1</sup>), the slope is around -1, whereas in the high  $q$  region (0.1 to 0.3 Å<sup>-1</sup>), the slope is around -4. **c–f**, Full range 2D <sup>1</sup>H–<sup>1</sup>H NOESY NMR spectra recorded with 1 s mixing times of PM6:BTP-TO2 in d-CF (**c**), PM6:BTP-TC8 in d-CF (**d**)

PM6:BTP-TO2 in d-Xylene (**e**), PM6:BTP-TC8 in d-Xylene (**f**), where corresponding regions are highlighted using square boxes (the red region corresponds to the intra-molecular interactions, whereas the blue region corresponds to the intermolecular interactions), with all the curves collected at room temperature. The axes  $F_2$  (ppm) corresponds to horizontal  $x$  axes and  $F_1$  (ppm) corresponds to vertical  $y$  axes. The  $F_1$  and  $F_2$  axes of 2D <sup>1</sup>H–<sup>1</sup>H NOESY NMR spectra are a function of the <sup>1</sup>H NMR frequencies/chemical shifts in the same scale.

Supplementary Table 1), a feature that is expected to have no negative impact on the magnitude of voltage losses from the perspective of the energy offsets. We notice that BTP-TC8 is also known as Y11 in literature; we follow the International Union of Pure and Applied Chemistry (IUPAC) rules to facilitate the comparison between BTP-TC8 and our BTP-TO2.

We start by investigating the molecular behaviour and aggregation states of the pure BTP-TO2 and BTP-TC8 acceptor molecules in various solvents (chloroform, chlorobenzene, toluene and p-xylene) and combine experimental investigations with theoretical calculations. We find that our acceptor materials dissolve well (with no aggregation) in a range of different solvents (at concentrations of 20 mg ml<sup>-1</sup>). Both BTP-TO2 and BTP-TC8 demonstrate similar ultraviolet–visible (UV–vis) absorption spectra in different solvents, in terms of peak positions and shapes (as shown in Fig. 1). This consistency points to the fact that changing solvents does not significantly alter the aggregation states or molecular self-assembly behaviours within the solutions (at concentrations of 20 mg ml<sup>-1</sup>) for both molecules<sup>40</sup>. Whereas there are only slight variations in the absorption spectra of different solutions, there are distinct redshifts observed during the transition from solution to film, a phase characterized by significant aggregation or molecular self-assembly behaviours (Fig. 1b,c). To further evaluate the aggregation behaviour of BTP-TO2 and BTP-TC8 in different solvents, we employed temperature-dependent UV–vis absorption spectroscopy. Over a wide range of temperatures (Supplementary Figs. 7 and 8), both BTP-TC8 and BTP-TO2 solutions exhibit nearly identical peak positions (around 750 nm) and similar shapes; the negligible impact of temperature on the absorption spectra indicates that the molecules are well dissolved at room temperature. The small-angle neutron scattering (SANS) analysis suggests a general absence of large-sized aggregation

(typically tens of nanometres) in solution, as no specific morphological aggregated structures are predominantly observed in either BTP-TO2 or BTP-TC8 solutions at concentrations of 20 mg ml<sup>-1</sup> (Supplementary Fig. 9 and Supplementary Tables 2 and 3). However, some degree of aggregation may still be present, though not prominent in the overall analysis. Additionally, theoretical determinations of the Flory–Huggins parameters based on all-atom molecular dynamics (AA-MD) simulations<sup>41</sup> demonstrate that the critical points for the various solvents consistently exceed the interaction parameters ( $\chi$ ) between the solvent and either BTP-TO2 or BTP-TC8 (Fig. 1d) at concentrations of 20 mg ml<sup>-1</sup>, which rationalizes that both BTP-TO2 and BTP-TC8 can well dissolve. To summarize this section, the pure small-molecule acceptors BTP-TO2 and BTP-TC8 dissolve well in a variety of solvents without exhibiting significant large-sized solvent-induced aggregation behaviours.

Despite the absence of aggregation of BTP-TO2 and BTP-TC8 in a range of solvents at concentrations of 20 mg ml<sup>-1</sup>, the molecular conformational responses are intricately correlated with the solvent employed. Notably, BTP-TO2 exhibits a greater intrinsic insensitivity to conformational changes across different solvents compared to BTP-TC8, as evidenced by two-dimensional <sup>1</sup>H–<sup>1</sup>H Nuclear Overhauser Effect Spectroscopy (2D <sup>1</sup>H–<sup>1</sup>H NOESY NMR) analysis (Supplementary Fig. 10). The conformational stability of BTP-TO2, as opposed to BTP-TC8, is demonstrated by negligible changes in the off-diagonal signals within the aromatic hydrogen region (6.5–10.0 ppm), whereas the significant changes observed for BTP-TC8 suggest that different intra- and inter-molecular interactions exist in different solutions. Furthermore, the calculated intra-molecular radial pair distribution functions,  $g(r)$ , for the BTP-TO2 molecules in AA-MD simulated solutions—spanning side chains, core unit and end units—also indicate small changes across various solvents. In contrast, the BTP-TC8 molecules



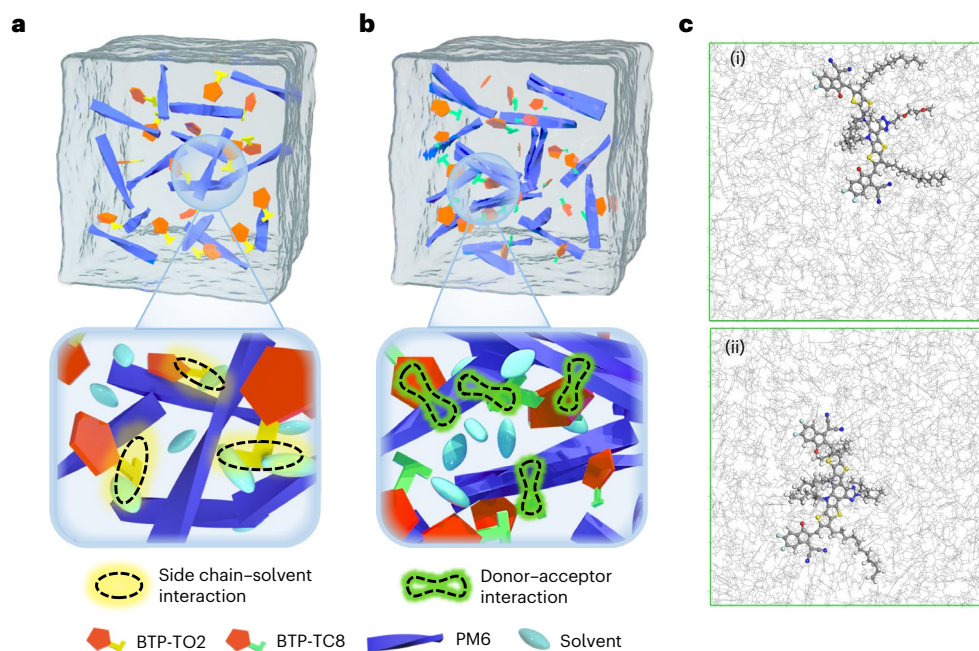


**Fig. 3 | Illustration of the rigid molecular conformation controlled by strong interactions between OEG side chains and solvents. a, b,** Cartoons providing a schematic visualization of the differences that are found between the BTP-TO2- and BTP-TC8-based systems. **c,** Molecular dynamics snapshots of BTP-TO2 (i),

BTP-TC8 (ii) molecular conformations in PX solution: the OEG side chain of BTP-TO2 consistently extends out linearly within the surrounding solvents, whereas the side chain of BTP-TC8 is entangled with its backbone.

show notable solvent-dependent variability in  $g(r)$ , especially between atoms in the end units and hydrogen atoms in the side chains (Supplementary Discussion 1 and Supplementary Fig. 11). These results imply that there occur minimal intra-molecular interactions between the OEG side chain and the other BTP-TO2 moieties, which favour the preservation of the BTP-TO2 molecular conformation. Thus, our designed OEG side chains ensure strong interactions between the small-molecule acceptor and its surrounding solvent molecules (Supplementary Discussion 2, Supplementary Scheme 1 and Supplementary Table 4) without altering the conformation of the acceptor molecules in the various solutions, which highlights the intrinsic stability of the BTP-TO2 molecular conformation across various solvents.

### Solution states for PM6:BTP-TO2 and PM6:BTP-TC8 blends

Bearing in mind the distinct molecular conformation behaviours of BTP-TO2 and BTP-TC8 in various solvents (despite their similar solubility), we now turn to their blends with the polymer donor poly[(2,6-(4,8-bis(5-(2-ethylhexyl)-4-fluorothiophen-2-yl) benzo[1,2-b:4,5-b'] dithiophene))-co-(1,3-di(5-thiophene-2-yl)-5,7-bis(2-ethylhexyl) benzo[1,2-c:4,5-c']dithiophene-4,8-dione (PM6)]. We carried out SANS measurements to provide quantitative insights into the molecular conformations and aggregation states of PM6:BTP-TC8 and PM6:BTP-TO2 blends in different solvents. The SANS curves are fitted using a flexible cylinder model (Fig. 2 and Supplementary Fig. 12), where the power-law decay, observed in the  $q$  region from 0.005 to 0.3  $\text{\AA}^{-1}$ , follows  $I(q) \approx q^{-D}$ . This parameter,  $D$ , representing the fractal dimension, reflects the geometry of the component conformations. In the intermediate  $q$  region (0.007 to 0.1  $\text{\AA}^{-1}$ ), the scattering intensity follows a  $q^{-1}$  evolution vs  $q$ , while it follows a  $q^{-4}$  behaviour in the high  $q$  region (0.1 to 0.3  $\text{\AA}^{-1}$ ). This behaviour is observed when polymer chains form cylindrical/rod-like conformations in solution<sup>42</sup>. By fitting the intermediate  $q$  range (0.01–0.1  $\text{\AA}^{-1}$ ) scattering curves after subtracting the incoherent scattering background, we find that the  $D$  values fall within the range of  $-1$  to  $-2$  in all PM6:BTP-TO2 and PM6:BTP-TC8 solutions, indicating a semi-flexible chain properties in solutions<sup>43</sup>. Under appropriate model

fitting, relatively large Kuhn lengths and large radius of gyration ( $R_g$ ) exhibit in various PM6:BTP-TO2 solutions, indicating a more rigid polymer molecular conformation (Supplementary Table 5 and Supplementary Discussion 3). These results are also in agreement with the minimal changes in PM6 absorption spectra observed upon mixing with BTP-TO2 but significant differences in PM6:BTP-TC8 system (Supplementary Fig. 13). Considering all these analyses, it can be concluded that in PM6:BTP-TO2 solutions, the components are weakly sensitive to solvents in contrast to what is observed in the PM6:BTP-TC8 solutions.

Analysis of 2D  $^1\text{H}$ - $^1\text{H}$  NOESY NMR spectra reveals a fundamental difference for the solvent sensitivities in PM6:BTP-TC8 and PM6:BTP-TO2 blends, as there exists a very distinct range of intermolecular interactions between donors and acceptors. For PM6:BTP-TO2, in both chloroform and xylene solutions (Fig. 2c,e), the correlation signals (among all aromatic hydrogens and all detected off-diagonal regions) primarily arise from intra-molecular interactions within BTP-TO2 molecules, with minimal interactions with the PM6 polymer chains. These correlation patterns reasonably support a model where the steric hindrance caused by the strong aliphatic OEG chains–solvent interactions, in turn, results in essentially weak BTP-TO2-PM6 intermolecular interactions. In contrast, in PM6:BTP-TC8 solutions, 2D  $^1\text{H}$ - $^1\text{H}$  NOESY NMR spectra display different broadened off-diagonal signals in different solutions, pointing not only to BTP-TC8-BTP-TC8 intra-molecular interactions but also to substantial BTP-TC8-PM6 intermolecular interactions (the blue region highlighted in Fig. 2d,f), thereby leading to the heterogeneity in the solution state of the different mixtures with BTP-TC8. In addition, the similar solution and film absorption spectra of the PM6 component processed from different solvents (Supplementary Fig. 14) rule out any direct impact of the solvents themselves on the PM6 molecular conformation and aggregation behaviours.

The results above allow us to gain a clear understanding of how the characteristics of the polymer/non-fullerene interactions in solution can provide solvent insensitivity in the case of BTP-TO2. As shown schematically in Fig. 3, in the solution state, the strong intermolecular interactions between the BTP-TO2 side chains and the solvent molecules effectively ensure that the conformation of the BTP-TO2

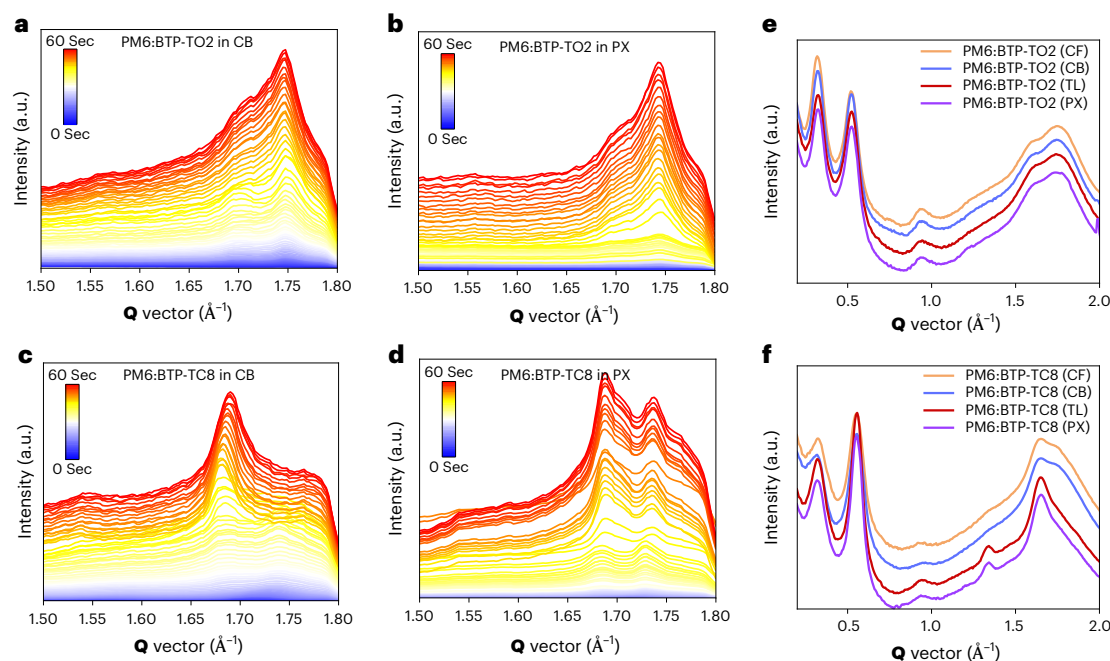


**Fig. 4 | Deposition dynamics of the components from solution to film and the crystalline properties of blend films. a–d,** Line cuts of in situ spin coating 2D GIWAXS profiles with the integrated azimuthal angle range from  $-10^{\circ}$  to  $10^{\circ}$  (out-of-plane direction) for PM6:BTP-TO2 in CB (a), PM6:BTP-TO2 in PX (b), PM6:BTP-TC8 in CB (c), PM6:BTP-TC8 in PX (d), in going from solution to film. **e, f,** Line cuts

of 2D GIWAXS profiles with the integrated azimuthal angle range from  $-10^{\circ}$  to  $10^{\circ}$  (out-of-plane direction) for PM6:BTP-TO2 films fabricated by using CF, TL, PX and CB (e), PM6:BTP-TC8 films fabricated by using CF, TL, PX and CB (f). The scale of the y axis is linear. The scale of the  $Q$  vector is the scattering wave vector transfer.

molecules does not undergo significant changes in different solvents. Also, the weak intermolecular interactions between polymer donor and BTP-TO2 molecules help maintain a rod-like conformation of the polymers, mitigating twisting and entanglement of the polymer chains in different solvents. As a result, a high degree of solvent tolerance is achieved in the PM6:BTP-TO2 solutions.

### Molecular assembly dynamics and final film structures

Having rationalized the molecular conformations and intermolecular interactions in solution, we now address the question of whether these distinct features are maintained during solvent evaporation and thin-film formation, whose kinetics play a key role in determining the molecular self-assembly and nano-scale phase structures in the final film.

In situ spin coating grazing incidence wide-angle X-ray scattering (GIWAXS) analysis reveals that within PM6:BTP-TO2 blends, both PM6 and BTP-TO2 maintain their molecular packing and interaction states throughout the film deposition process (Fig. 4). Specifically, for PM6:BTP-TO2 blends, in the out-of-plane direction, the  $\pi$ - $\pi$  stacking diffraction of PM6 (010),  $1.75 \text{ \AA}^{-1}$ , consistently exceeds that of BTP-TO2 (010),  $1.70 \text{ \AA}^{-1}$ , during the initial seconds of solvent evaporation, indicating a higher deposition rate for PM6 irrespective of the solvent (as illustrated in Fig. 4a,b and Supplementary Fig. 15). This difference in deposition rates ensures that PM6 (with its rigid conformation) precipitates preferentially and forms a matrix, with BTP-TO2 filling in the remaining spaces without changing the conformation of the PM6 chains. In contrast, the PM6:BTP-TC8 blends show distinct solvent sensitivity. For instance, in blends processed from chlorobenzene, BTP-TC8 tends to deposit before PM6 (Fig. 4c,d), whereas in the case of toluene, PM6 deposits first, as depicted in Supplementary Fig. 15. In other words, the non-uniform molecular packing and intermolecular interactions observed across various solutions for PM6:BTP-TC8 are further expressed during film formation kinetics. In addition, whereas

pristine BTP-TO2 shows a relatively stable molecular conformation in various solutions, the morphologies of the neat BTP-TO2 thin films display significant solvent dependence (Supplementary Fig. 16). These results demonstrate the importance of the rod-like conformation of PM6 in solution and its preferential precipitation during the film formation process in establishing the final solvent-insensitive blend film morphology.

All-atom molecular dynamics simulations provide a theoretical insight into the fundamental mechanisms behind these phenomena. We evaluated the cohesive energy density (CED), which allows us to quantify the various interactions among the components present in a given system. Importantly, we find that the CEDs between the solvents and the OEG side chains in BTP-TO2 are consistently higher than those among solvent molecules (Supplementary Table 6); this underlines the strong interactions between BTP-TO2 and solvent molecules, which we discussed above. In contrast, the CEDs between the solvent molecules and the branched alkyl chains in BTP-TC8 are smaller than those among solvent molecules, indicating weak interactions between BTP-TC8 and solvent molecules. Upon increasing the system concentration to simulate film formation kinetics, the BTP-TO2–solvent interactions remain strong and the BTP-TC8–solvent interactions remain weak (Supplementary Table 7). These results demonstrate that high CEDs between acceptor and solvent in the PM6:BTP-TO2 solution minimize the dependence of component deposition on the dynamics of solvent evaporation. In contrast, the weak interactions between branched alkyl chains and solvents in PM6:BTP-TC8 make the component deposition sensitive to the kinetics of solvent evaporation.

The solvent insensitivity of the PM6:BTP-TO2 blends in terms of both solution and film formation kinetics leads to a film morphology that is independent of the processing solvent. We employ static 2D GIWAXS for a quantitative assessment of the nano-scale morphological crystalline structures within the PM6:BTP-TO2 and PM6:BTP-TC8 films (Fig. 4e,f and Supplementary Figs. 17–19). In PM6:BTP-TO2 blends, the maximum fluctuation (obtained by subtracting the minimum value

from the maximum value across all blends) for both the lamellar (100) and  $\pi$ - $\pi$  stacking (010) peak positions is around  $0.02 \text{ \AA}^{-1}$ , whereas the maximum fluctuation for their coherence crystalline lengths (CCLs) is around 0.6 nm. In contrast, for PM6:BTP-TC8 blends, the maximum fluctuation for the lamellar (100) and  $\pi$ - $\pi$  stacking (010) peak positions is approximately  $0.04 \text{ \AA}^{-1}$ , with a maximum fluctuation of around 5.6 nm for their CCLs. These results indicate that the crystalline structure of PM6:BTP-TO2 films is relatively less sensitive to the solvents. This reduced sensitivity can be attributed to the preferred rod-like molecular conformation and weak donor-acceptor intermolecular interactions in solution states, as discussed above. The intrinsic properties of the solvents, such as boiling points and solvent volumes, might be responsible for the slight perturbations in the peak positions and CCLs in PM6:BTP-TO2 blends<sup>44</sup>. For semi-paracrystalline organic semiconductors, slight distortions in the crystalline structures are not supposed to significantly affect the electrical properties in functional devices<sup>45</sup>. The smaller CEDs make the molecular packing susceptible to the evaporation dynamics of different solvents in PM6:BTP-TC8 blends (Supplementary Tables 6 and 7 and Supplementary Discussion 4).

Actually, the intensity ratio is obviously similar between the out-of-plane  $\pi$ - $\pi$  stacking diffraction (010) of PM6 at  $1.75 \text{ \AA}^{-1}$  and that of BTP-TO2 at  $1.70 \text{ \AA}^{-1}$  in the PM6:BTP-TO2 blend films (Fig. 4e and Supplementary Fig. 20). Upon area integration across an azimuth angle  $\alpha$  ranging from  $10^\circ$  to  $45^\circ$ , we observe similar ratios of the  $\pi$ - $\pi$  stacking diffraction (010) intensities between PM6 and BTP-TO2 at any given azimuth angle (as detailed in Supplementary Scheme 1 and Supplementary Fig. 21), indicating that the relative crystallinity between PM6 and BTP-TO2 is independent of out-of-plane orientation. These molecular packing and spatial distribution findings align well with the component deposition kinetics that we discussed before. On the contrary, in the PM6:BTP-TC8 blend films, the  $\pi$ - $\pi$  stacking intensity ratio between PM6 and BTP-TC8 exhibits a strong dependence on solvents (Fig. 4f and Supplementary Fig. 21). Interestingly, the intensity of BTP-TC8 is stronger than PM6 in the blend film at every azimuthal angle, suggesting that the crystallinity of BTP-TC8 dominates the morphology.

Additionally, resonant soft x-ray scattering (RSOXS) (Supplementary Fig. 22 and Supplementary Table 8) is used to characterize the average phase separation and domain size in PM6:BTP-TO2 and PM6:BTP-TC8 blends, rather than focusing solely on the crystalline parts. From the RSOXS profiles, the corresponding long period of phase separation (relating to the centre-to-centre domain spacing) can be estimated from peak positions. All the centre-to-centre domain spacings for PM6:BTP-TO2 blends exhibit a statistically less sensitive trend to solvents, ranging from approximately 47.6 nm to 49.8 nm, compared to PM6:BTP-TC8 blends, which range from 53.3 nm to 76.6 nm. Similar insensitivity is also observed in the average domain sizes (calculated using the Scherrer equation), which range from 29.7 nm to 29.4 nm for PM6:BTP-TO2 blends and from 22.9 nm to 52.2 nm for PM6:BTP-TC8 blends. Grazing incidence small-angle X-ray scattering (GISAXS) further reveals the average acceptor domain size ( $2R_{g\text{-fractal}}$ ) and the intermixing domain size ( $\xi$ ) by fitting the profiles integrated along in-plane direction with the Debye-Anderson-Brumberger model and the fractal-like network model<sup>46,47</sup>. As shown in Supplementary Figs. 23 and 24, the average acceptor domain size and intermixing domain sizes in PM6:BTP-TO2 blends also exhibit statistically less sensitivity to various solvents compared to PM6:BTP-TC8 blends. It should be noted that the difference in values (such as average domain sizes) between RSOXS and GISAXS results primarily stems from the relative contrast of donor and acceptor components to hard and soft X-rays and the different fitting models used for different techniques. Overall, the solvent insensitivity of the PM6:BTP-TO2 blends in primary solutions, film formation dynamics and final thin films results in a statistically similar crystalline structure and average domain size. These results highlight that our morphological control strategy, that is, increasing the side chain-solvent interactions in conjunction with weak donor-acceptor

**Table 1 | Photovoltaic parameters of the OSCs based on different active layers under AM1.5 G 100 mW cm<sup>-2</sup> illumination**

Active layer <sup>a</sup>	V <sub>oc</sub> (V)	J <sub>sc</sub> (mA cm <sup>-2</sup> )	FF	PCE <sub>max</sub> (%) <sup>b</sup>
PM6:BTP-TO2 (chloroform)	0.87	27.05	80.56	19.07 (18.88 ± 0.19)
PM6:BTP-TO2 (chlorobenzene)	0.87	27.15	79.12	18.83 (18.65 ± 0.18)
PM6:BTP-TO2 (toluene)	0.87	27.24	80.43	19.13 (18.92 ± 0.21)
PM6:BTP-TO2 (p-xylene)	0.87	27.01	80.12	18.96 (18.79 ± 0.17)
PM6:BTP-TC8 (chloroform)	0.85	27.27	76.25	17.61 (17.41 ± 0.20)
PM6:BTP-TC8 (chlorobenzene)	0.82	25.08	71.24	14.65 (14.41 ± 0.24)
PM6:BTP-TC8 (toluene)	0.83	24.66	74.52	15.29 (15.07 ± 0.22)
PM6:BTP-TC8 (p-xylene)	0.82	24.70	71.11	14.39 (14.20 ± 0.19)

<sup>a</sup>All the optimized devices maintain a similar thickness of  $105 \pm 10$  nm. <sup>b</sup>Average and standard deviation data in brackets are obtained from 20 cells for each condition.

interactions in solution, enable us to achieve a solvent-insensitive morphology (for example, in terms of molecular packing, orientational distributions and average phase separation) of the resulting thin films, crucial for achieving consistent device performance.

## High and uniform device performance from various solvents

With the comprehensive appreciation we gained for the molecular conformations/interactions in solution and the film formation processes of PM6:BTP-TC8 and PM6:BTP-TO2 blends, we fabricated OSCs with the conventional structure corresponding to indium tin oxide (ITO)/[2-(9H-carbazol-9-yl) ethyl] phosphonic acid (2PACZ)/active layer/C<sub>60</sub>/2,9-dimethyl-4,7-diphenyl-1,10 phenanthroline (BCP)/Ag. Figure 5 and Table 1 display the current density-voltage (*J-V*) curves and photovoltaic parameters, respectively, of the optimized devices based on different active layers. The best PCE for the PM6:BTP-TC8 blend (17.61%, similar to previous reports<sup>12</sup>) is achieved when chloroform is used as processing solvent. However, upon switching to other solvents (regardless of whether they are halogenated or non-halogenated), the device efficiency significantly decreases; this points to the strong solvent dependence normally expected for organic photovoltaic blends. In stark contrast, the PM6:BTP-TO2-based devices maintain high average PCEs around 19.0% across different processing solvents (the fluctuation ratio is less than 2% obtained from 20 cells), with a champion PCE of 19.07% (certified at 19.06%; Supplementary Fig. 25 and Supplementary Table 9). The integrated current densities calculated from the external quantum efficiency (EQE) also match well the short-circuit current (*J<sub>sc</sub>*) values obtained from the *J-V* curves within deviations of ~3% (Supplementary Fig. 26). These results indicate that the PM6:BTP-TO2 blend, characterized by solvent-insensitive crystalline structures and average domain sizes, facilitates the formation of uniformly performing OSCs with a high tolerance to the nature of the processing solvents.

To validate the broad applicability of our solvent-insensitive design principles, we first considered the extension of the number of oxygen atoms in the OEG chains from two to three (to produce the new small molecule acceptor BTP-TO3; Supplementary Figs. 27–30). The elongated OEG side chains also show high interaction energies between BTP-TO3 and their surrounding solvent molecules, without affecting the molecular conformation (Supplementary Table 10 and Supplementary Fig. 31). The device parameters based on the PM6:BTP-TO3



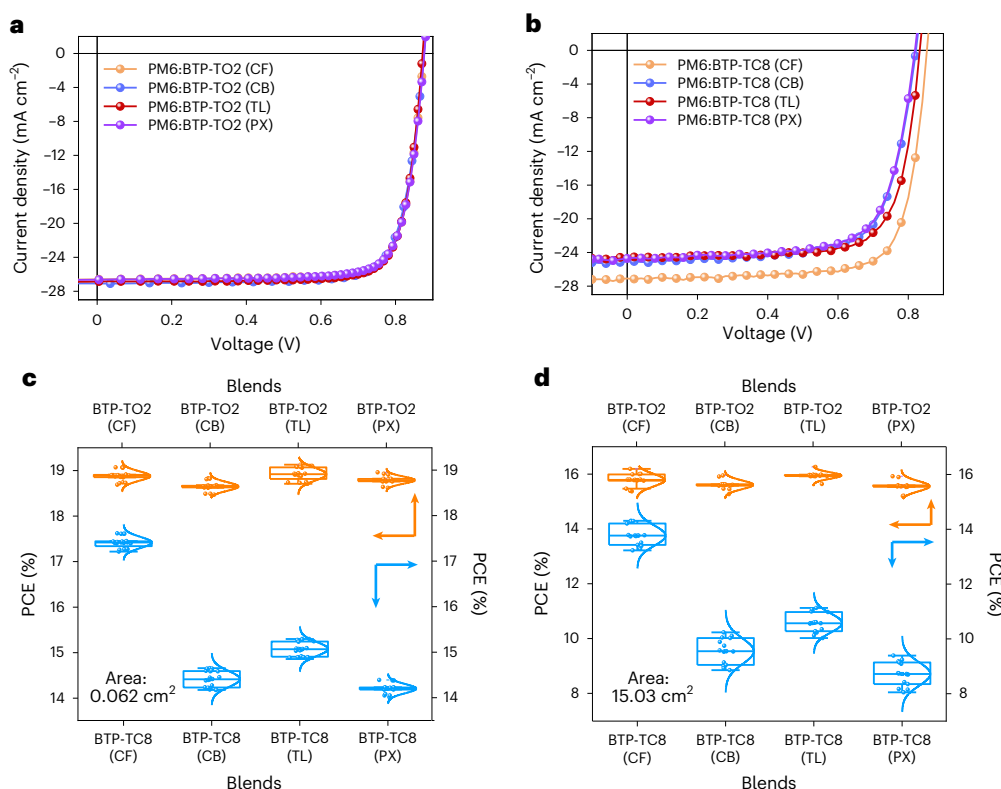


**Fig. 5 | Photovoltaic performance of the devices.** **a–c**,  $J$ – $V$  curves of PM6:BTP-TO2- (**a**) and PM6:BTP-TC8- (**b**) based OSCs processed with various solvents under the illumination of AM1.5 G  $100 \text{ mW cm}^{-2}$  and statistical PCEs distribution of small-scaled OSCs based on PM6:BTP-TO2 and PM6:BTP-TC8 processed with various solvents under the illumination of AM1.5 G  $100 \text{ mW cm}^{-2}$  (**c**). All the data are obtained from 20 cells for each condition. **d**, Statistical PCEs distribution of the OSC modules based on PM6:BTP-TO2 and PM6:BTP-TC8 processed with

various solvents under the illumination of AM1.5 G  $100 \text{ mW cm}^{-2}$ . All the data are obtained from 15 cells for each condition. For the box plots, the central line represents the median, the bounds of the box represent the interquartile range (25th and 75th percentiles) and the whiskers extend to the minimum and maximum values within 1.5 times the interquartile range. Outliers are shown as individual points.

blend also exhibit the same high tolerance to different solvents (Supplementary Fig. 32 and Supplementary Table 11). In addition, we also considered another type of small-molecule acceptor, ID-OEG-2F<sup>39</sup>, based on the well-studied indacenodithiophene (IDT) core to which one OEG side chain is attached. Importantly, when blended with PM6 and processed from different solvents, this acceptor also leads to similar parameters in conventional device structures (Supplementary Fig. 33 and Supplementary Table 12). All these results support the validity of our morphological design rules.

In addition to remarkable efficiencies, the similar morphologies of the PM6:BTP-TO2 blends processed from different solvents also result in similar stabilities. As shown in Supplementary Fig. 34, all PM6:BTP-TO2 OSCs processed with four different solvents exhibit high stability with  $T_{80}$  over 1,200 h under continuous operation at the maximum power point under  $100 \text{ mW cm}^{-2}$  white light-emitting diode (LED) illumination. In contrast, PM6:BTP-TC8 OSCs processed from different solvents demonstrate different degrees of stability, consistent with their solvent-dependent morphologies. The best stability for PM6:BTP-TC8 is obtained for the chloroform-processed devices, with an additional decay of around 10% compared with PM6:BTP-TO2 under the same conditions.

Solvent insensitivity of the PM6:BTP-TO2 blends, coupled with very high device performance (in terms of both efficiency and stability), encouraged us to develop large-area photovoltaic modules. As a demonstration, we fabricated a  $5 \times 5 \text{ cm}^2$  active layer using the blade coating method (Supplementary Fig. 35) and assembled modules comprising eight series-connected individual cells with a total active area of  $15.64 \text{ cm}^2$  in ambient atmosphere (Supplementary Fig. 36).

As shown in Fig. 5d, Supplementary Table 13 and Supplementary Fig. 37, various PM6:BTP-TO2-based devices processed in both halogenated and non-halogenated solvents demonstrate similar PCEs of around 16.10%. In contrast, the PM6:BTP-TC8-based OSC module processed in chloroform shows a lower PCE of 14.31%, which further decreases to around 10% after switching to other solvents. Consistently, the map of light-beam-induced current generated by scanning the devices with a 632 nm laser shows that the photocurrent distribution in the PM6:BTP-TO2-based modules is stronger and more uniform than that in the modules based on PM6:BTP-TC8 (Supplementary Fig. 38). To the best of our knowledge, the 16.26% PCE of the toluene-processed device is one of the highest values among non-halogenated solvent-processed OSC modules with an active area  $>10 \text{ cm}^2$  (Supplementary Fig. 39 and Supplementary Table 14). These results manifest the importance of our materials design principles towards commercial development of OSC modules using non-halogenated solvents.

## Conclusion

In summary, we demonstrate high-performance large-area OSCs processed from a range of different solvents. Our work highlights that the solution states, which can be manipulated by careful design of the molecules, play a determining role on the morphology (and hence the performance) of OSCs. On the basis of our comprehensive understanding, we provide design rules for effective control of morphological structures in blends: to enhance the interaction between the side chain of the small-molecule acceptors and the solvent, ensuring that acceptors maintain a stable and persistent molecular conformation in various solutions; to weaken the intermolecular interactions



between the polymer donor and the non-fullerene acceptor in solution, promoting the rod-like conformation of the polymer donor and its preferential precipitation and ensuring that the film formation dynamics has little impact on the blend film morphology. Our materials design principles offer important guidance for the chemical structural design of novel donor and acceptor materials, paving the way towards high-performance OSCs processed from environmentally friendly solvents for commercialization.

## Methods

### Materials

ITO glass with a sheet resistance of  $15 \Omega \text{ sq}^{-1}$  and a transmittance of 86% and  $\text{C}_{60}$  were purchased from Advanced Election Technology Co. PM6 and 2-(5,6-difluoro-3-oxo-2,3-dihydro-1H-inden-1-ylidene) malononitrile (IC-2F) were purchased from Solarmer Materials Inc. The weight-average molecular weight is 90 kDa, whereas the molecular weight distribution (PDI) is 2.06. BTP-TC8 was purchased from eFlexPV Limited. CF (99%), TL (99%), PX (99%) and CB (99%) were purchased from J&K. 2PACZ and BCP were purchased from Xi'an Yuri Solar Co. All the materials were used as received without further purification.

### Material synthesis

**Preparation of BTP-2OG-CHO.** BTP-2OG-CHO was synthesized according to the reported method<sup>3,38</sup>.

**Preparation of BTP-TO2.** BTP-2OG-CHO (111.27 mg, 0.10 mmol) and IC-2F (0.14 g, 0.40 mmol) were added in a flask, and chloroform (45 ml) with pyridine (1 ml) were used to dissolve them. The mixture was stirred at 65 °C overnight. After cooling to room temperature, the mixture was poured into methanol and filtered. The residue was purified with column chromatography on silica gel using CF as the eluent to obtain a dark blue solid BTP-TO2 (98.63 mg, 64.17% yield).  $^1\text{H}$  NMR (600 MHz,  $\text{CDCl}_3$ )  $\delta$  9.16 (s, 2H), 8.60–8.54 (m, 2H), 7.73–7.68 (m, 2H), 5.04–5.00 (s, 2H), 4.80–4.67 (m, 4H), 4.33–4.32 (t, 2H), 3.75–3.68 (t, 6H), 3.57–3.53 (t, 2H), 3.26–3.24 (s, 4H), 2.01 (m, 2H), 1.99 (m, 4H), 1.56–1.52 (m, 4H), 1.26 (m, 30H), 1.17–0.94 (m, 22H), 0.89–0.63 (m, 12H).  $^{13}\text{C}$  NMR (150 MHz,  $\text{CDCl}_3$ )  $\delta$  186.10, 158.94, 153.93, 153.41, 158.55, 144.91, 137.89, 136.45, 136.22, 135.23, 134.45, 133.44, 133.16, 129.60, 119.52, 115.05, 114.67, 112.43, 111.78, 77.18, 76.76, 71.37, 70.62, 69.46, 68.21, 55.75, 55.41, 42.68, 40.28, 31.88, 31.26, 29.84, 29.30, 27.56, 23.20, 22.65, 14.08, 13.70, 10.15. MS (MALDI-TOF)  $m/z$  calculated. For ( $\text{C}_{87}\text{H}_{97}\text{F}_4\text{N}_9\text{O}_4\text{S}_4$ ): 1,535.65. Found: 1,535.275.

**Preparation of BTP-TO3.** BTP-3OG-CHO (115.68 mg, 0.10 mmol) and IC-2F (0.14 g, 0.40 mmol) were added in a flask, and chloroform (45 ml) with pyridine (1 ml) were used to dissolve them. The mixture was stirred at 65 °C overnight. After cooling to room temperature, the mixture was poured into methanol and filtered. The residue was purified with column chromatography on silica gel using CF as the eluent to give a dark blue solid BTP-TO3 (99.36 mg, 62.84% yield).  $^1\text{H}$  NMR (600 MHz,  $\text{CDCl}_3$ )  $\delta$  9.16 (s, 2H), 8.60–8.54 (m, 2H), 7.73–7.68 (m, 2H), 5.04–5.00 (s, 2H), 4.80–4.67 (m, 4H), 4.33–4.31 (t, 2H), 3.75–3.68 (t, 6H), 3.57–3.53 (t, 4H), 3.26–3.20 (s, 4H), 2.01 (m, 2H), 1.99 (m, 4H), 1.56–1.52 (m, 4H), 1.26 (m, 30H), 1.13–0.94 (m, 22H), 0.89–0.63 (m, 12H).  $^{13}\text{C}$  NMR (150 MHz,  $\text{CDCl}_3$ )  $\delta$  186.10, 158.94, 153.93, 153.41, 144.91, 137.89, 136.45, 136.22, 135.23, 134.45, 133.44, 133.16, 129.60, 119.52, 115.05, 114.67, 112.43, 111.78, 77.18, 76.76, 71.37, 70.62, 69.46, 68.21, 55.41, 55.41, 42.68, 40.28, 31.88, 31.26, 29.84, 29.62, 29.30, 27.56, 23.20, 22.65, 14.08, 13.70, 10.15. MS (MALDI-TOF)  $m/z$  calculated. For ( $\text{C}_{89}\text{H}_{101}\text{F}_4\text{N}_9\text{O}_5\text{S}_4$ ): 1,579.67. Found: 1,579.005.

**NMR spectra measurements.**  $^1\text{H}$  and  $^{13}\text{C}$  NMR spectra were measured using a Varian Mercury-400 NMR.  $^{13}\text{C}$  NMR spectra were obtained under simultaneous  $^1\text{H}$  decoupling (WALTZ-16). High-resolution NMR measurements were recorded on a Bruker 400 MHz Avance NEO

spectrometer at Larmor frequency  $\nu(^1\text{H}) = 400.132$  MHz. For  $^1\text{H}$ - $^1\text{H}$  NOESY NMR with gradient pulses in mixing time measurements were conducted with the width of 90° pulse 16.5  $\mu\text{s}$  and relaxation delay 6.5 s. Spectral width in both frequency dimensions was 14 ppm. The indirect detection period  $t_1$  consisted of 512 increments each made of 32 scans. Dried  $d_5$ -chlorobenzene (99.9%) was used as solvent and for calibration of  $^1\text{H}$  NMR isotropic chemical shift. The temperature was kept constant at  $298 \pm 0.2$  K with a BVT 3000 temperature unit during measurements. All samples were dissolved in chlorobenzene- $d_5$  at room temperature in inert (Ar) atmosphere.

**High-resolution MALDI-TOF measurements.** The positive-ion mode matrix-assisted laser desorption/ionization time-of-flight instrument (Bruker) was employed for the mass characterization.

**Electrical measurements.** The  $J$ - $V$  characteristics of the devices were measured with a computer-controlled Keithley 2450 Source Measure Unit under AM 1.5 G illumination ( $100 \text{ mW cm}^{-2}$ ) from a SS-F5-3A solar simulator (Enli Technology Co.) without any preconditioning. The light intensity was calibrated by a standard silicon solar cell (SRC-00178, calibrated by Enli Technology Co.) before testing. The  $J$ - $V$  curves of small-area devices were measured in forward scan (from  $-0.2$  V to 1.2 V) mode with the scan step length of 0.02 V and a dwell time of 1 ms for each voltage. The  $J$ - $V$  curves of large-area modules were measured in forward scan (from  $-1$  V to 11 V) mode with the scan step length of 0.02 V and a dwell time of 1 ms for each voltage. The cells were placed face up in the glovebox and were illuminated from the bottom during testing at room temperature. The EQE spectra were obtained using a QE-R3011 solar cell spectral response measurement system (Enli Technology, Co.). The light intensity at each wavelength was also calibrated with a standard silicon solar cell (RCS103011-E, calibrated by Enli Technology Co.). By calculating the  $J_{sc}$  from EQE based on the solar simulator spectral for the reference silicon cell and our solar cells, the mismatch factor ( $M$ ) was close to unity ( $M > 0.98$ ). The aperture areas of the masks used for testing small-area devices and large-area modules are 0.0628  $\text{cm}^2$  and 15.03  $\text{cm}^2$ , respectively.

**CV measurements.** For CV experiments, the compound was fully dissolved in anhydrous chloroform and then the solution was deposited onto the work electrode surface to form a thin solid film. CV traces were measured on an IM6 electrochemical workstation (Zahner Zennium, Germany) at a scan rate of 50  $\text{mV s}^{-1}$  using tetrabutylammonium tetrafluoroborate ( $\text{Bu}_4\text{NBF}_4$ ) as the supporting electrolyte. A glassy carbon electrode, a Pt wire and an  $\text{Ag}/\text{AgNO}_3$  electrode were used as the working, counter and reference electrodes, respectively.

**UV-vis absorption spectra measurements.** The transmittance and absorption spectra were measured with an ultraviolet spectrometer (Agilent Technologies Cary 5000 UV-vis-NIR).

**Molecular dynamics simulations.** The all-atom (AA) molecular dynamics (MD) simulations were carried out with the LAMMPS package<sup>48</sup> and the Optimized Potentials for Liquid Simulations-All Atom (OPLS-AA) force field<sup>49–51</sup>. The generalized OPLS-AA force field was re-parameterized by the following procedure: (1) the atomic partial charges were evaluated via fitting the electrostatic potential determined by density functional theory calculations at the  $\omega\text{B97XD}/\text{cc-pVTZ}$  level of theory; (2) the bond lengths and angles were taken from the molecular geometries optimized at the  $\omega\text{B97XD}/6-31\text{G}(\text{d},\text{p})$  level of theory, with the harmonic force constants kept unchanged; and (3) the dihedral (between the core and the end unit of BTP-TC8 or BTP-TO2) parameters were fitted on the basis of the torsion potentials evaluated at the  $\omega\text{B97XD}/6-31\text{G}(\text{d},\text{p})$  level. The density functional theory calculations were performed with the Gaussian 09 package<sup>48</sup>.

**SANS measurements.** Solution samples were loaded into Banjo Hellma cells for SANS measurement on the GP-SANS CG-2 beamline at the High Flux Isotope Reactor, Oak Ridge National Laboratory in Oak Ridge, Tennessee<sup>52</sup>. The neutron wavelength was  $\lambda = 4.75 \text{ \AA}$  with spread  $\Delta\lambda/\lambda = 0.13$ , and three configurations with sample-to-detector distances of 1, 7 and 19 m were used to cover the scattering wavevector  $q$  range  $0.003 - 0.7 \text{ \AA}^{-1}$ . All measurements were conducted at ambient conditions, and the total scattering cross sections were calibrated by pre-calibrated porous silica and corrected for empty cell scattering, sample transmission, thickness, detector sensitivity and instrument noise. The azimuthally isotropic two-dimensional (2D) scattering patterns were then reduced to one-dimensional (1D) intensity  $I$  as a function of  $q$ <sup>53</sup>.

**Static, in situ 2D GIWAXS and GISAXS measurements.** The 2D GIWAXS measurement was conducted at beamline 7.3.3 at the Advanced Light Source at Lawrence Berkeley National Lab. The samples were illuminated with 10 keV radiation ( $\lambda = 1.24 \text{ \AA}$ ) at an incident angle ( $\alpha$ ) of  $0.12^\circ$ . The beam size was  $300 \text{ \mu m}$  (height)  $\times$   $700 \text{ \mu m}$  (width). The scattering signal was captured on a Pilatus 2 M ( $172 \text{ \mu m}$  pixel size, file format EDF,  $1,475 \times 1,679$  pixels) located 282 mm from the sample. The GISAXS measurement was also conducted at beamline 7.3.3, except that the sample-to-detector distance was increased from 282 mm to 2.5 m to access the lower  $q$  range. The raw data were integrated with the Igor Pro NIKA GIWAXS software and further processed using Xi-Cam.

**RSoXS measurement.** RSoXS measurements were performed at beamline 11.0.1.2 at the Advanced Light Source. Samples for RSoXS measurement were prepared on a PEDOT:PSS modified silicon substrate under the same conditions as those used for device fabrication, then transferred by floating in water to a  $1.5 \text{ mm} \times 1.5 \text{ mm}$ , 100 nm thick  $\text{Si}_3\text{N}_4$  membrane supported by a  $5 \text{ mm} \times 5 \text{ mm}$ , 200- $\mu\text{m}$ -thick silicon frame (Norcada Inc.) 2D scattering patterns were collected on an in-vacuum S5 CCD camera (Princeton Instrument PI-MTE). The sample detector distance was calibrated from diffraction peaks of a triblock copolymer poly (isoprene-*b*-styrene-*b*-2-vinyl pyridine), which has a known spacing of 391  $\text{\AA}$ . The beam size at the sample is approximately  $100 \text{ \mu m}$  to  $200 \text{ \mu m}$ . The median domain spacing is calculated from the  $2\pi/q$ , where  $q$  here corresponds to half of the total scattering intensity.

**Stability measurements.** Operational stability measurements of the OSCs were conducted by using the white light LED array under continuous illumination of the simulating intensity of  $100 \text{ mW cm}^{-2}$  (spectra region: 410–850 nm, Suzhou D&R Instruments Co. PVL1-G8001M-32B) at maximum power point ( $\text{N}_2$  atmosphere, temperature around 45–55 °C) and the currents were recorded with time by the Keithley 2400 source meter. Small-area devices ( $0.0988 \text{ cm}^2$ ) were used for the stability measurements.

**Device fabrication.** Conventional structure of ITO/2PACZ/active layer/ $\text{C}_{60}$ /BCP/Ag were fabricated. ITO-coated glass substrates were rinsed with deionized water, acetone and isopropyl alcohol by ultrasonication, sequentially, and then dried with  $\text{N}_2$ . After that, the 2PACZ layer was spin coated on top of ITO substrates at 2,000 rpm and then dried at 120 °C for 15 min. Then it was transferred into a  $\text{N}_2$ -filled glovebox immediately. Active layer precursor solutions were prepared with donor: acceptor ratio 1:1.2 (w/w, 11.5 mg  $\text{ml}^{-1}$  of donor, in various solvents: chloroform, chlorobenzene, toluene, *p*-xylene, *o*-xylene). Subsequently, the active layer precursor solutions were spin coated onto the 2PACZ-coated substrate at around 2,500 rpm and then annealed at 100 °C for 10 min. The active layer thicknesses were controlled at  $105 \pm 10 \text{ nm}$ . A  $\text{MoO}_3$  layer (10 nm) and an Al film (100 nm) were thermally deposited on the active layer by vacuum evaporation under  $3 \times 10^{-4} \text{ Pa}$ .

The large-area modules were fabricated with an conventional structure of ITO/PEDOT:PSS/active layer/ $\text{C}_{60}$ /BCP/Ag. ITO-coated

glass substrates were rinsed with deionized water, acetone and isopropyl alcohol by ultrasonication, sequentially, then dried with  $\text{N}_2$ . After that, the PEDOT:PSS layer was deposited through blade coating at  $20 \text{ mm s}^{-1}$  on pre-cleaned ITO-coated glass and annealed at 150 °C for 20 min in atmospheric air. The active layer was blade coated from various solvents with a coating velocity of  $20 \text{ mm s}^{-1}$ , and a gap height of 20  $\mu\text{m}$  in the air to form an ~100-nm-thick active layer without any post-processing. Next, 10-nm-thick  $\text{C}_{60}$  and 5-nm-thick BCP layers were deposited by thermal evaporation under  $1 \times 10^{-6} \text{ mbar}$ . Then shadow masking was used to complete the module and make the Ag to ITO interconnection between adjacent cells. The active area of the module was defined by the shadow mask and the aperture mask as  $15.03 \text{ cm}^2$ .

### Reporting summary

Further information on research design is available in the Nature Portfolio Reporting Summary linked to this article.

### Data availability

All data generated or analysed during this study are included in the published article, its Supplementary Information and Source Data files. Source data are provided with this paper.

### References

1. Lin, Y. et al. An electron acceptor challenging fullerenes for efficient polymer solar cells. *Adv. Mater.* **27**, 1170–1174 (2015).
2. Yuan, J. et al. Single-junction organic solar cell with over 15% efficiency using fused-ring acceptor with electron-deficient core. *Joule* **3**, 1140–1151 (2019).
3. Wang, J. et al. Tandem organic solar cells with 20.6% efficiency enabled by reduced voltage losses. *Natl Sci. Rev.* **10**, nwad085 (2023).
4. Jiang, Y. et al. Non-fullerene acceptor with asymmetric structure and phenyl-substituted alkyl side chain for 20.2% efficiency organic solar cells. *Nat. Energy* **9**, 975–986 (2024).
5. Zhu, L. et al. Single-junction organic solar cells with over 19% efficiency enabled by a refined double-fibril network morphology. *Nat. Mater.* **21**, 656–663 (2022).
6. Chen, Z. et al. 20.2% efficiency organic photovoltaics employing a  $\pi$ -extension quinoxaline-based acceptor with ordered arrangement. *Adv. Mater.* **36**, 2406690 (2024).
7. Günes, S., Neugebauer, H. & Sariciftci, N. S. Conjugated polymer-based organic solar cells. *Chem. Rev.* **107**, 1324–1338 (2007).
8. Baran, D. et al. Reducing the efficiency–stability–cost gap of organic photovoltaics with highly efficient and stable small molecule acceptor ternary solar cells. *Nat. Mater.* **16**, 363–369 (2017).
9. Cui, Y. et al. Wide-gap non-fullerene acceptor enabling high-performance organic photovoltaic cells for indoor applications. *Nat. Energy* **4**, 768–775 (2019).
10. Classen, A. et al. The role of exciton lifetime for charge generation in organic solar cells at negligible energy-level offsets. *Nat. Energy* **5**, 711–719 (2020).
11. Maimaris, M. et al. Sub-10-fs observation of bound exciton formation in organic optoelectronic devices. *Nat. Commun.* **13**, 4949 (2022).
12. Liu, S. et al. High-efficiency organic solar cells with low non-radiative recombination loss and low energetic disorder. *Nat. Photonics* **14**, 300–305 (2020).
13. Kraabel, B. et al. Ultrafast photoinduced electron transfer in conducting polymer–buckminsterfullerene composites. *Chem. Phys. Lett.* **213**, 389–394 (1993).
14. Yu, G. & Heeger, A. J. Charge separation and photovoltaic conversion in polymer composites with internal donor/acceptor heterojunctions. *J. Appl. Phys.* **78**, 4510–4515 (1995).

15. Halls, J. J. M. et al. Efficient photodiodes from interpenetrating polymer networks. *Nature* **376**, 498–500 (1995).
16. Yu, G., Gao, J., Hummelen, J. C., Wudl, F. & Heeger, A. J. Polymer photovoltaic cells: enhanced efficiencies via a network of internal donor–acceptor heterojunctions. *Science* **270**, 1789–1791 (1995).
17. Firdaus, Y. et al. Long-range exciton diffusion in molecular non-fullerene acceptors. *Nat. Commun.* **11**, 5220 (2020).
18. Chen, Z. et al. Ultrafast hole transfer and carrier transport controlled by nanoscale-phase morphology in nonfullerene organic solar cells. *J. Phys. Chem. Lett.* **11**, 3226–3233 (2020).
19. Shi, Y. et al. Small reorganization energy acceptors enable low energy losses in non-fullerene organic solar cells. *Nat. Commun.* **13**, 3256 (2022).
20. Karuthedath, S. et al. Intrinsic efficiency limits in low-bandgap non-fullerene acceptor organic solar cells. *Nat. Mater.* **20**, 378–384 (2021).
21. Peet, J. et al. Efficiency enhancement in low-bandgap polymer solar cells by processing with alkane dithiols. *Nat. Mater.* **6**, 497–500 (2007).
22. Lee, J. K. et al. Processing additives for improved efficiency from bulk heterojunction solar cells. *J. Am. Chem. Soc.* **130**, 3619–3623 (2008).
23. Ruderer, M. A. et al. Solvent-induced morphology in polymer-based systems for organic photovoltaics. *Adv. Funct. Mater.* **21**, 3382–3391 (2011).
24. Zhang, R. et al. Molecular orientation and phase separation by controlling chain segment and molecule movement in P3HT/N2200 blends. *Macromolecules* **49**, 6987–6996 (2016).
25. Bavel van, S. S., Sourty, E., With de, G. & Loos, J. Three-dimensional nanoscale organization of bulk heterojunction polymer solar cells. *Nano Lett.* **9**, 507–513 (2009).
26. Wei, Y. et al. Binary organic solar cells breaking 19% via manipulating the vertical component distribution. *Adv. Mater.* **34**, 2204718 (2022).
27. Zhang, R. et al. To reveal the importance of the crystallization sequence on micro-morphological structures of all-crystalline polymer blends by in situ investigation. *ACS Appl. Mater. Interfaces* **13**, 21756–21764 (2021).
28. Jiang, K. et al. Pseudo-bilayer architecture enables high-performance organic solar cells with enhanced exciton diffusion length. *Nat. Commun.* **12**, 468 (2021).
29. Wang, Y. et al. Origins of the open-circuit voltage in ternary organic solar cells and design rules for minimized voltage losses. *Nat. Energy* **8**, 978–988 (2023).
30. Zuo, L. et al. Dilution effect for highly efficient multiple-component organic solar cells. *Nat. Nanotechnol.* **17**, 53–60 (2022).
31. Luginbuhl, R. B. et al. Resolving atomic-scale interactions in nonfullerene acceptor organic solar cells with solid-state NMR spectroscopy, crystallographic modelling, and molecular dynamics simulations. *Adv. Mater.* **34**, 2105943 (2022).
32. Liang, Z. et al. Optimization requirements of efficient polythiophene: nonfullerene organic solar cells. *Joule* **4**, 1278–1295 (2020).
33. Wang, R. et al. Rational tuning of molecular interaction and energy level alignment enables high-performance organic photovoltaics. *Adv. Mater.* **31**, 1904215 (2019).
34. Liu, Y. et al. Aggregation and morphology control enables multiple cases of high-efficiency polymer solar cells. *Nat. Commun.* **5**, 5293 (2014).
35. Qin, Y., Xu, Y., Peng, Z., Hou, J. & Ade, H. Low temperature aggregation transitions in N3 and Y6 acceptors enable double-annealing method that yields hierarchical morphology and superior efficiency in nonfullerene organic solar cells. *Adv. Funct. Mater.* **30**, 2005011 (2020).
36. Khasbaatar, A. et al. From solution to thin film: molecular assembly of  $\pi$ -conjugated systems and impact on (opto) electronic properties. *Chem. Rev.* **123**, 8395–8487 (2023).
37. Zhu, L. et al. Efficient organic solar cell with 16.88% efficiency enabled by refined acceptor crystallization and morphology with improved charge transfer and transport properties. *Adv. Energy Mater.* **10**, 1904234 (2020).
38. Meng, B. et al. Replacing alkyl with oligo(ethylene glycol) as side chains of conjugated polymers for close  $\pi$ - $\pi$  stacking. *Macromolecules* **48**, 4357–4363 (2015).
39. Chen, H. et al. A guest-assisted molecular-organization approach for >17% efficiency organic solar cells using environmentally friendly solvents. *Nat. Energy* **6**, 1045–1053 (2021).
40. Reichenberger, M. et al. Controlling aggregate formation in conjugated polymers by spin-coating below the critical temperature of the disorder–order transition. *J. Polym. Sci. Part B* **56**, 532–542 (2018).
41. Wang, T. & Brédas, J.-L. Organic photovoltaics: understanding the preaggregation of polymer donors in solution and its morphological impact. *J. Am. Chem. Soc.* **143**, 1822–1835 (2021).
42. Khasbaatar, A. et al. Solution aggregate structures of donor polymers determine the morphology and processing resiliency of non-fullerene organic solar cells. *Chem. Mater.* **35**, 2713–2729 (2023).
43. Gao, M. et al. Tuning the solution aggregation and molecular order for efficient and thermally stable polymer solar cells. *Energy Environ. Sci.* **16**, 5822–5831 (2023).
44. Liu, F. et al. Efficient polymer solar cells based on a low bandgap semi-crystalline DPP polymer-PCBM blends. *Adv. Mater.* **24**, 3947–3951 (2012).
45. Noriega, R. et al. A general relationship between disorder, aggregation and charge transport in conjugated polymers. *Nat. Mater.* **12**, 1038–1044 (2013).
46. Cai, G. et al. Deuteration-enhanced neutron contrasts to probe amorphous domain sizes in organic photovoltaic bulk heterojunction films. *Nat. Commun.* **15**, 2784 (2024).
47. Liu, H. et al. Dual-additive-driven morphology optimization for solvent-annealing-free all-small-molecule organic solar cells. *Adv. Funct. Mater.* **33**, 2303307 (2023).
48. Plimpton, S. Fast parallel algorithms for short-range molecular dynamics. *J. Comput. Phys.* **117**, 1–19 (1995).
49. Jorgensen, W. L. & Tirado-Rives, J. The OPLS [optimized potentials for liquid simulations] potential functions for proteins, energy minimizations for crystals of cyclic peptides and crambin. *J. Am. Chem. Soc.* **110**, 1657–1666 (1988).
50. Dahlgren, M. K., Schyman, P., Tirado-Rives, J. & Jorgensen, W. L. Characterization of biaryl torsional energetics and its treatment in OPLS all-atom force fields. *J. Chem. Inf. Model.* **53**, 1191–1199 (2013).
51. Jackson, N. E. et al. Conformational order in aggregates of conjugated polymers. *J. Am. Chem. Soc.* **137**, 6254–6262 (2015).
52. Heller, W. T. et al. The suite of small-angle neutron scattering instruments at Oak Ridge National Laboratory. *J. Appl. Cryst.* **51**, 242–248 (2018).
53. Heller, W. T. et al. drtsans: the data reduction toolkit for small-angle neutron scattering at Oak Ridge National Laboratory. *SoftwareX* **19**, 101101 (2022).

## Acknowledgements

We thank O. Inganäs, H. Zhang, Y. Li and N. Jain for insightful discussions and inputs. We thank C. Wang for RSoXS measurement and data analysis. This work was supported by the Swedish Strategic Research Foundation through a Future Research Leader programme to F.G. (FFL 18-0322); the National Natural Science Foundation of China to Yaowen Li (52325307); the Swedish Government Strategic Research



Area in Materials Science on Functional Materials at Linköping University (faculty grant number SFO-Mat-LiU #2009-00971); the Wallenberg Initiative Materials Science for Sustainability WISE; Olle Engkvists Stiftelse; the US Office of Naval Research and US Office of Naval Research Global under grant number N62909-23-1-2043; the Office of Naval Research under award numbers N00014-20-1-2110 and N00014-24-1-2114; and the University of Arizona Institute of Energy Solutions and Office for Research, Innovation, and Impact for support via the Arizona Technology and Research Initiative Fund. The 2D NMR measurement and analysis was supported by the Grant Agency of the Czech Republic (grant GA24-10199S). T.W. and Q.J. acknowledge supports by the National Natural Science Foundation of China (number 52130101) and the National Key R&D Program of China (grant number 2023YFB3003001), ‘Xiaomi Young Scholar’ project. H.C. acknowledges the National Natural Science Foundation of China (22309129). The static/in situ 2D GIWAXS data were acquired at beamlines 7.3.3 at the Advanced Light Source, which is supported by the Director, Office of Science, Office of Basic Energy Sciences, of the US Department of Energy (DE-AC02-05CH11231). Y.D. and A.K. acknowledge support by the Office of Naval Research under grant number N00014-22-1-2202. This research used resources at the High Flux Isotope Reactor, a DOE Office of Science User Facility operated by the Oak Ridge National Laboratory. The beam time was allocated to CG2 on proposal number IPTS-31199.1. F.G. is a Wallenberg Scholar. H.L. and X.L. would like to acknowledge the support from the Research Grants Council (RGC) of Hong Kong (number 14304723).

## Author contributions

R.Z. conceived the ideas and supervised the project with F.G. and Yaowen Li. R.Z. performed the investigation and characterization of the solutions and films under the supervision of F.G. T.W., S.N., Q.J., V.C. and J.-L.B. conducted the density functional theory calculations and molecular dynamic simulations. R.Z. designed the new acceptor materials, C.H. and J.D. synthesized them. R.Z., A.H.C. and C.Z. measured the in situ/static 2D GIWAXS and performed the data analysis. A.K. and Y.D. performed the static 2D GIWAXS data analysis. R.Z. and L.H. measured the SANS and performed the data analysis. J.Z. and W.C. performed the absorption spectrum of solutions and films. L.K., S.A. and J.B. measured the 2D NMR and performed the results analysis. Y.H. fabricated the small-area devices and performed the device stability. B.Z. fabricated the large-area devices. R.Z., H.L. and X.L. analysed the 2D GISAXS data. R.Z. wrote the manuscript. F.G.,

J.-L.B and Yongfang Li revised the manuscript. All authors discussed the results and commented on the final manuscript.

## Funding

Open access funding provided by Linköping University.

## Competing interests

The authors declare no competing interests.

## Additional information

**Supplementary information** The online version contains supplementary material available at <https://doi.org/10.1038/s41560-024-01678-5>.

**Correspondence and requests for materials** should be addressed to Tonghui Wang, Yaowen Li or Feng Gao.

**Peer review information** *Nature Energy* thanks Feng He, Peter Müller-Buschbaum and the other, anonymous, reviewer(s) for their contribution to the peer review of this work.

**Reprints and permissions information** is available at [www.nature.com/reprints](http://www.nature.com/reprints).

**Publisher's note** Springer Nature remains neutral with regard to jurisdictional claims in published maps and institutional affiliations.

**Open Access** This article is licensed under a Creative Commons Attribution 4.0 International License, which permits use, sharing, adaptation, distribution and reproduction in any medium or format, as long as you give appropriate credit to the original author(s) and the source, provide a link to the Creative Commons licence, and indicate if changes were made. The images or other third party material in this article are included in the article's Creative Commons licence, unless indicated otherwise in a credit line to the material. If material is not included in the article's Creative Commons licence and your intended use is not permitted by statutory regulation or exceeds the permitted use, you will need to obtain permission directly from the copyright holder. To view a copy of this licence, visit <http://creativecommons.org/licenses/by/4.0/>.

© The Author(s) 2024

<sup>1</sup>Department of Physics, Chemistry and Biology (IFM), Linköping University, Linköping, Sweden. <sup>2</sup>Laboratory of Advanced Optoelectronic Materials, College of Chemistry, Chemical Engineering and Materials Science, Soochow University, Suzhou, China. <sup>3</sup>Key Laboratory of Automobile Materials, Ministry of Education, School of Materials Science and Engineering, Jilin University, Changchun, China. <sup>4</sup>Institute of Macromolecular Chemistry of the Czech Academy of Sciences, Prague, Czech Republic. <sup>5</sup>Neutron Scattering Division, Oak Ridge National Laboratory, Oak Ridge, TN, USA. <sup>6</sup>Department of Chemical and Biomolecular Engineering, University of Illinois Urbana-Champaign, Urbana, IL, USA. <sup>7</sup>Department of Chemistry and Biochemistry, University of Arizona, Tucson, AZ, USA. <sup>8</sup>Department of Chemistry, University of Illinois Urbana-Champaign, Urbana, IL, USA. <sup>9</sup>Advanced Light Source, Lawrence Berkeley National Laboratory, Berkeley, CA, USA. <sup>10</sup>Department of Physics, Chinese University of Hong Kong, Hong Kong, China. <sup>11</sup>Beijing National Laboratory for Molecular Sciences, CAS Key Laboratory of Organic Solids, Institute of Chemistry, Chinese Academy of Sciences, Beijing, China. <sup>12</sup>Wallenberg Initiative Materials Science for Sustainability, Department of Physics, Chemistry and Biology, Linköping University, Linköping, Sweden. ✉e-mail: [twang@jlu.edu.cn](mailto:twang@jlu.edu.cn); [ywli@suda.edu.cn](mailto:ywli@suda.edu.cn); [feng.gao@liu.se](mailto:feng.gao@liu.se)



## Solar Cells Reporting Summary

Nature Portfolio wishes to improve the reproducibility of the work that we publish. This form is intended for publication with all accepted papers reporting the characterization of photovoltaic devices and provides structure for consistency and transparency in reporting. Some list items might not apply to an individual manuscript, but all fields must be completed for clarity.

For further information on Nature Research policies, including our [data availability policy](#), see [Authors & Referees](#).

### ► Experimental design

Please check the following details are reported in the manuscript, and provide a brief description or explanation where applicable.

#### 1. Dimensions

- Area of the tested solar cells  Yes  No Described in Methods, section "Electrical measurements". The area of tested small area solar cells is 0.0628 cm<sup>2</sup>, while 15.03 cm<sup>2</sup> for large area solar cells
- Method used to determine the device area  Yes  No Determined by aperture of the masks as stated in "Electrical measurements". The aperture areas of the masks used for testing small area devices and large-area modules are 0.0628 cm<sup>2</sup> and 15.03 cm<sup>2</sup>, respectively.

#### 2. Current-voltage characterization

- Current density-voltage (J-V) plots in both forward and backward direction  Yes  No The devices have been tested in forward (from negative to positive) direction.
- Voltage scan conditions  Yes  No Described in Methods, section "Electrical measurements". The J-V curves of small-area devices were measured in forward scan (from -0.2 V to 1.2 V) mode with the scan step length of 0.02 V and a dwell time of 1 ms for each voltage. The J-V curves of large-area modules were measured in forward scan (from -1 V to 11 V) mode with the scan step length of 0.02 V and a dwell time of 1 ms for each voltage.
- Test environment  Yes  No Described in Methods, section "Electrical measurements". The cells were placed faceup in the glove box and were illuminated from the bottom during testing at room temperature.
- Protocol for preconditioning of the device before its characterization  Yes  No No preconditioning protocol.
- Stability of the J-V characteristic  Yes  No We performed long-term efficiency tracking of the solar cells at nitrogen under continuous illumination of the simulating intensity of 100 mW cm<sup>-2</sup> (spectra region: 410-850 nm, Suzhou D&Rinstruments Co., Ltd. PVLT-G8001M-32B). The temperature is around 45-55 °C.

#### 3. Hysteresis or any other unusual behaviour

- Description of the unusual behaviour observed during the characterization  Yes  No No unusual behaviour.
- Related experimental data  Yes  No No unusual behaviour.

## 4. Efficiency

External quantum efficiency (EQE) or incident photons to current efficiency (IPCE)

Yes  
 No

The EQE is Provided in Supplementary Fig. 26, 32b, 33b.

A comparison between the integrated response under the standard reference spectrum and the response measure under the simulator

Yes  
 No

All the  $J_{sc}$  values obtained from the J-V curves (Table 1, Fig. 5, Supplementary Fig. 26, 32, 33, 37, and Supplementary Table 9, 11, 12, 13) are compared with the integrated current densities (Supplementary Fig. 26, 32b, 33b), showing approximately 3% error.

For tandem solar cells, the bias illumination and bias voltage used for each subcell

Yes  
 No

No tandem solar cells are involved in this manuscript.

## 5. Calibration

Light source and reference cell or sensor used for the characterization

Yes  
 No

Described in Methods, section "Electrical measurements". The J-V curves of the devices are measured with a computer-controlled Keithley 2450 Source Measure Unit under AM1.5G illumination (100 mW cm<sup>-2</sup>) from a SS-F5-3A solar simulator (Enli Technology, Co., Ltd) without any preconditioning. The EQE spectra are obtained using a QE-R3011 solar cell spectral response measurement system (Enli Technology, Co., Ltd).

Confirmation that the reference cell was calibrated and certified

Yes  
 No

Described in Methods, section "Electrical measurements". For J-V characterization, The light intensity is calibrated by a standard silicon solar cell (SRC-00178, calibrated by Enli Technology Co., Ltd) before testing. For EQE characterization, The light intensity at each wavelength is also calibrated with a standard silicon solar cell (RCS103011-E, calibrated by Enli Technology Co., Ltd).

Calculation of spectral mismatch between the reference cell and the devices under test

Yes  
 No

Described in Methods, section "Electrical measurements". By calculating the  $J_{sc}$  from EQE based on the solar simulator spectral for the reference silicon cell and our solar cells, the mismatch factor (M) is close to unity ( $M > 0.98$ ).

## 6. Mask/aperture

Size of the mask/aperture used during testing

Yes  
 No

Described in Methods, section "Electrical measurements". The aperture areas of the masks used for testing small area devices and large-area modules are 0.0628 cm<sup>2</sup> and 15.03 cm<sup>2</sup>, respectively.

Variation of the measured short-circuit current density with the mask/aperture area

Yes  
 No

All J-V curves are tested with a mask.

## 7. Performance certification

Identity of the independent certification laboratory that confirmed the photovoltaic performance

Yes  
 No

Devices with around 5.80 mm<sup>2</sup> area were certified at Shanghai Institute of Microsystem and Information Technology, Chinese Academy of Science.

A copy of any certificate(s)

Yes  
 No

We provided the certified results in Supplementary Fig. 25.

## 8. Statistics

Number of solar cells tested

Yes  
 No

We tested at least 15 cells for both small-area and large-area devices.

Statistical analysis of the device performance

Yes  
 No

We provided statistical analysis in Table 1, Supplementary Table 9, 11, 12, 13.

## 9. Long-term stability analysis

Type of analysis, bias conditions and environmental conditions

- Yes
- No

Described in Methods, section "Stability measurements". The operational stability of devices is conducted by using the white light LED array under continuous illumination of the simulating intensity of 100 mW cm<sup>-2</sup> (spectra region: 410-850 nm, Suzhou D&Rinstruments Co., Ltd. PVL-T-G8001M-32B) at MPP (N<sub>2</sub> atmosphere, temperature around 45-55 °C) and the currents were recorded with time by the Keithley 2400 source meter.